Realization of kagome lattice and superconductivity in topological electrides

Yu-Hao Wei,[1,*] Hao-Dong Liu,[2,3,*] Da-Shuai Ma,[4,5,†] Hong-Kuan Yuan,[1] Bao-Tian Wang,[2,3,‡] and Min-Quan Kuang[1,§]

[1]*Chongqing Key Laboratory of Micro & Nano Structure Optoelectronics, and School of Physical Science and Technology, Southwest University, Chongqing 400715, People's Republic of China*

[2]*Institute of High Energy Physics, Chinese Academy of Sciences, Beijing 100049, People's Republic of China*

[3]*Spallation Neutron Source Science Center, Dongguan 523803, People's Republic of China*

[4]*Institute for Structure and Function & Department of Physics & Chongqing Key Laboratory for Strongly Coupled Physics, Chongqing University, Chongqing 400044, People's Republic of China*

[5]*Center of Quantum Materials and Devices, Chongqing University, Chongqing 400044, People's Republic of China*

(Received 4 February 2024; revised 16 May 2024; accepted 30 July 2024; published 13 August 2024)

Realization of kagome lattice, and hence achieving specific performance, is a challenging issue in condensed matter physics. The corner-sharing triangles of kagome lattice are normally comprised of real atoms occupying certain Wyckoff sites. Here, we propose that the excess electrons in layered electrides Mg_3N and Mg_3O build the two-dimensional kagome lattices. The interstitial electrons further contribute to the nontrivial band topology, i.e., the Dirac points and the Dirac nodal lines in Mg_3N and Mg_3O. Further, the in-plane coupling between the electronic orbitals and the atomic vibrational modes dominate the electron-phonon coupling, and yield superconducting critical temperatures approaching 2.0 and 2.2 K for Mg_3N and Mg_3O, respectively. This work proposes a feasible scheme to construct kagome lattices by interstitial quasiatoms and provides a promising platform to explore the superconductivity and nontrivial band topology in kagome electrides.

DOI: 10.1103/PhysRevB.110.054511

I. INTRODUCTION

Kagome materials have attracted much research interest due to their exotic electronic, magnetic, topological, and superconducting properties. As for the ideal two-dimensional (2D) kagome nets, the emergent Dirac point (DP), flat band, and van Hove singularity (vHS) reveals the deep physics hidden behind the material itself, such as band topology and electronic correlation [1]. Referring to real kagome materials, the geometric frustration of corner-sharing triangles normally varies with element compositions, which produces fruitful phenomena in terms of magnetism [2–5], spin liquid [6,7], spin ice [8–10], quantum spin Hall effect (QSHE) [11–13], anomalous Hall effect (AHE) [2,14,15], quantum anomalous Hall effect (QAHE) [16,17], nontrivial topological states [5,16,18–21], pair density wave (PDW) [22,23], charge density wave (CDW) [3,4,24–28], nematic order [26,27,29,30], and superconductivity [26,27,31–35]. Significantly, the coexistence of multiple orders suggests kagome lattice is a solid ground to investigate the intertwined states [3,25–27,31,32,34,36,37]. Thus, more kagome materials candidates are desired to explore the underlying mechanisms.

It is noticeable that the kagome sublattice in most of the reported kagome materials such as A_xB_y (A = Mn, Fe, Co, K, Rb, Cs; B = Sn, Ge, Bi; x:y = 1:1, 1:2, 3:1 and 3:2) [18,34,38–40] and $A_xB_yC_z$ (A = K, Rb, Cs, Sc, Y, La, S; B = V, Nb, Ta, B, Ti; C = Sb, Sn, Rh, Bi, Co; x:y:z = 1:2:3, 1:3:5, 1:6:6 and 2:2:3) [2,14,20,21,26,37,41,42] is made up by real atoms occupying specific Wyckoff sites. On the other hand, one notes that electrides, where excess electrons taking up the crystal interstitial sites can exhibit analogous characters to real atoms [43], have broad applications in catalysis [44,45], ion batteries [46,47], optical devices [48], spintronics [49,50], and superconductivity [51–56]. Then, one may ask whether there are any materials with specific properties where kagome lattices are built by the excess electrons rather than the real atoms. Here, we propose Mg_3N and Mg_3O as stable topological electrides with 2D kagome lattices constructed by the interstitial electrons. The electron-phonon coupling (EPC) between the Mg atoms and interstitial quasiatoms (ISQs) make a major contribution to the superconductivity, where the superconducting critical temperature T_c reaches 2.0 and 2.2 K for Mg_3N and Mg_3O, respectively.

In this work, the binary compounds Mg_3N and Mg_3O were identified as stable electrides by the phonon dispersion and *ab initio* molecular dynamics (AIMD) simulations (Fig. S1 in the Supplemental Material (SM) [57]). Remarkably, the excess electrons take up the crystal interstitial space and form 2D kagome lattices in the Mg layers (Fig. 2). Moreover, these ISQs dominate the bands near the Fermi level E_F and contribute to the topological states of Mg_3N (DPs) and Mg_3O [Dirac nodal lines (DNLs)] (Fig. 3). The in-plane EPC between the electronic orbitals and the atomic vibrational modes is much stronger than that of the out of plane (Fig. 4). The T_c calculated upon the Allen-Dynes-modified McMillan formula [58,59] is 2.0 and 2.2 K for Mg_3N and Mg_3O (Table I), respectively. These findings pave an alternative route to realize

*These authors contributed equally to this work.
†Contact author: madason.xin@gmail.com
‡Contact author: wangbt@ihep.ac.cn
§Contact author: mqkuang@swu.edu.cn

TABLE I. The calculated lattice constants a and c (Å), the electronic DOS at the Fermi level $N(E_F)$ (states/eV), the strength of EPC λ, $\omega_{\log}$ (K) and T_c (K) for Mg_3N and Mg_3O.

Electride	a	c	$N(E_F)$	λ	$\omega_{\log}$	T_c
Mg_3N	5.388	5.729	3.176	0.460	234.78	2.0
Mg_3O	5.386	5.402	2.959	0.467	241.71	2.2

kagome lattices in elecrides and will facilitate future research on the potential intertwined orders in topological kagome electrides.

II. COMPUTATIONAL METHODS

The first-principles calculations were performed by the Vienna *ab initio* simulation package (VASP) based on the density functional theory (DFT) [60,61]. The Perdew-Burke-Ernzerhof (PBE) function with projector-augmented wave (PAW) pseudopotential within the generalized gradient approximation (GGA) was adopted to treat the exchange correlation potentials [62,63]. The cutoff energy of the plane wave and the force tolerance were set to 500 eV and −0.01 eV/Å, respectively. The convergence accuracy of the self-consistent iteration was selected as 1×10^{-6} eV/atom, and the k-point grid was set to $9 \times 9 \times 9$. The plane wave cutoff energy and k mesh were respectively increased to 800 eV and $19 \times 19 \times 19$ for precise description of the electron localized function (ELF) and partial charge density (PCD). Phonon spectra were obtained using the $2 \times 2 \times 2$ supercell by the PHONOPY code [64] within density functional perturbation theory (DFPT) approach [65]. The AIMD simulations were performed in the framework of the Nose-Hoover thermostat ensemble. The topological states were demonstrated by the WANNIERTOOLS (WT) package [66], where the tight-binding method was employed with the maximally localized Wannier functions (MLWFs) [67,68]. Since the elements involved in both compounds are very light, the spin-orbit coupling (SOC) effect was ignored. The SOC effect was also excluded in the phonon-related computations, because the SOC is less important in describing the vibration and superconductivity [33,69].

As for the superconducting properties, the QUANTUM ESPRESSO (QE) package [70] was adopted to perform the DFT calculations, in which the PAW pseudopotentials under the PBE scenario [62] were utilized. In detail, the cutoff energy for the wave functions and charge density were set as 100 and 800 Ry, respectively. Phonon dispersion was calculated by the DFPT method [65], in which a denser $18 \times 18 \times 18$ k-point grid and a $6 \times 6 \times 6$ q-point mesh were applied for the EPC calculations. According to the Migdal-Eliashberg equations [71,72], the magnitude of the EPC λ_{qv}, which describes the contribution to λ from individual phonon modes, can be evaluated by

$$\lambda_{qv} = \frac{\gamma_{qv}}{\pi h N(E_F)\omega_{qv}^2}, \tag{1}$$

where γ_{qv} is the phonon linewidth, ω_{qv} stands for the frequency of a lattice vibration with crystal momentum q at the branch v, and $N(E_F)$ represents the density of states at the Fermi level. Besides, the phonon linewidth γ_{qv} can be written as

$$\gamma_{qv} = \frac{2\pi\omega_{qv}}{\Omega_{BZ}} \sum_{k,n,m} \left|g^v_{kn,k+qm}\right|^2 \delta(\epsilon_{kn} - \epsilon_F)\delta(\epsilon_{k+qm} - \epsilon_F), \tag{2}$$

where Ω_{BZ} is the volume of the Brillouin zone (BZ), n and m are the Kohn-Sham orbitals, ϵ_{kn} and ϵ_{k+qm} are the Kohn-Sham energies, and ϵ_F is the Fermi energy. The EPC matrix element $g^v_{kn,k+qm}$ can be self-consistently acquired with the linear response theory. Then, the cumulative frequency dependent EPC function $\lambda(\omega)$ can be obtained by

$$\lambda(\omega) = 2\int_0^\omega \frac{\alpha^2F(\omega)}{\omega} d\omega, \tag{3}$$

where the Eliashberg electron-phonon spectral function $\alpha^2F(\omega)$ is

$$\alpha^2F(\omega) = \frac{1}{2\pi N(E_F)} \sum_{qv} \frac{\gamma_{qv}}{\omega_{qv}} \delta(\omega - \omega_{qv}). \tag{4}$$

As a result, the T_c can be derived as

$$T_c = \frac{\omega_{\log}}{1.2} \exp\left[-\frac{1.04(1+\lambda)}{\lambda - \mu^*(1+0.62\lambda)}\right], \tag{5}$$

in which μ^* is the effective screened Coulomb repulsion constant with a typical value of 0.1 [73,74], and $\omega_{\log}$ is the logarithmic average frequency in terms of

$$\omega_{\log} = \exp\left[\frac{2}{\lambda}\int_0^\infty \frac{d\omega}{\omega}\alpha^2F(\omega)\log\omega\right]. \tag{6}$$

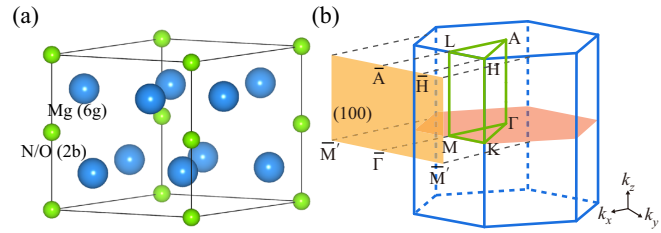

FIG. 1. (a) Crystal structure of Mg_3N and Mg_3O, where Mg and N (O) occupy the 6*g* and 2*b* Wyckoff sites, respectively. (b) The first Brillouin zone with high symmetry points and the projected (001) surface.

III. RESULTS AND DISCUSSION

Mg_3N and Mg_3O have the anti-$TiCl_3$ structure with space group $P6_3/mcm$ (No. 193) [Fig. 1(a)], which is similar to Cs_3O and Ba_3N [75], where alkaline-earth metal and nonmetal atoms occupy the 6*g*: $(x, x, \frac{3}{4})$ and 2*b*: $(0, 0, \frac{1}{2})$ Wyckoff sites, respectively. As tabulated in Table I, the calculated lattice constants are $a = b = 5.388$ Å (5.386 Å) and $c = 5.729$ Å (5.402 Å) for Mg_3N (Mg_3O). Based on the optimized structures, the computed phonon spectra along the selected high symmetry lines [see Fig. 1(b)] are displayed in Figs. S1(a) and (c) for Mg_3N and Mg_3O, respectively. The absence of imaginary frequency mode indicates that both Mg_3N and Mg_3O are dynamical stable. As shown in Figs. S1(b) and (d), the AIMD simulations evaluated the thermodynamic stability of Mg_3N and Mg_3O at room temperature (300 K). Then, we compute

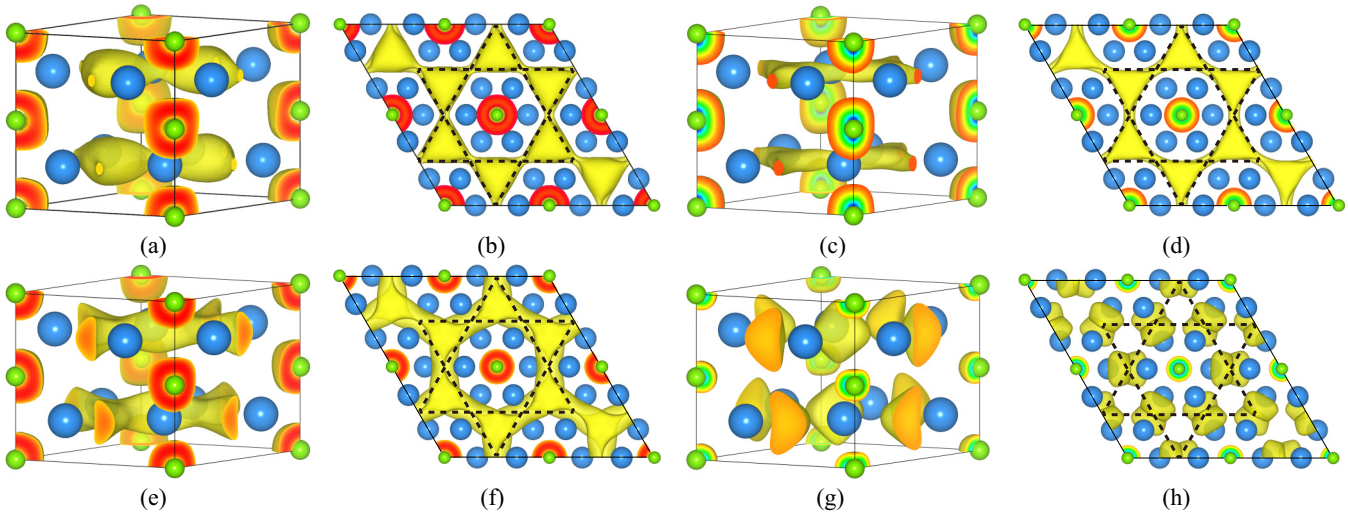

FIG. 2. The calculated ELF and PCD of Mg_3N and Mg_3O. Side view of the ELF for Mg_3N (a) and Mg_3O (e) with a same isosurface 0.67 e/Å^3. The corresponding top view for the $2 \times 2 \times 2$ supercell is displayed in (b) and (f), respectively. Side view of the PCD for Mg_3N (c) and Mg_3O (g) with an isovalue 0.009 e/Å^3 and 0.013 e/Å^3, respectively (see also Fig. S3 [57]). (d) and (h) correspond to the top view of the $2 \times 2 \times 2$ supercell, respectively. The PCD is calculated for the color bands that cross the Fermi level in Figs. 3(a) and 3(h).

the formation energy by $E_f = (E_{bulk} - 6\mu_{Mg} - 2\mu_{N/O})/8$. Here μ_{Mg} and $\mu_{N/O}$ are the energies of each Mg and N/O atom in their most stable elemental crystal/gas, while E_{bulk} is the total energy of Mg_3N and Mg_3O unit cells. The calculated E_f of Mg_3N and Mg_3O are -0.238 and -1.084 eV per atom, demonstrating the preference formation of Mg_3N and Mg_3O rather than the pure Mg and N/O phases. As shown in Fig S2, Mg_3N and Mg_3O are above the convex hull [57,76,77]. Then, one can infer that these two electrides are metastable and might be experimentally synthesized by designing suitable conditions and methods.

The ELF displayed in Figs. 2(a) and 2(e) clearly reveal that anions localize around the nonmetal atoms and distribute in the crystal interstitial space within the Mg layers of Mg_3N and Mg_3O. The localized electrons around nonmetal atoms can ascribe to the larger electronegativities of N (∼3.04) and O (∼3.44) than that of Mg (∼1.31) [78]. Noticeably, as presented in Figs. 2(b) and 2(f), the interstitial anions provided by excess electrons of Mg atoms build 2D kagome lattices for Mg_3N and Mg_3O. Combing with the PCDs for these bands that cross the Fermi surface [79–81] (Figs. 2(c), 2(d), 2(g), and 2(h), and Fig S3 [57]), one can treat Mg_3N and Mg_3O as electrides [82]. Though there is slight differences in morphology of ELFs and PCDs between Mg_3N and Mg_3O, which might be due to variations in crystal and electronic structures that arise from the different element compositions, both Mg_3N and Mg_3O can be regarded as kagome electrides [54,83].

Actually, the different element compositions indeed have some effects on the electronic properties of Mg_3N and Mg_3O. As shown in Figs. 3(a) and 3(h), several bands cross the Fermi level, indicating the metallic character of Mg_3N and Mg_3O. The characteristic features of kagome bands [54,84] can be revealed by the DPs that are highlighted by dashed circles in Figs. 3(a) and 3(h) for Mg_3N and Mg_3O, respectively. However, these DPs are well above the Fermi level that is not conducive to experimental observation. Then, we focus on the bands below the Fermi level and the topological elements are marked by solid circles in Figs. 3(a) and 3(h), respectively. To fully illustrate the electronic properties, the irreducible representations (irreps) of the little group at distinct $\boldsymbol{k}$ points in the BZ are obtained [85]. As for Mg_3N, the little group of the high symmetry H point $(\frac{1}{3}, \frac{1}{3}, \frac{1}{2})$ has three generating elements, i.e., S_3^+, C_{21}'', and PT. Here, S_3^+ denotes $\{S_3^+|000\}$, C_{21}'' indicates $\{C_{21}''|00\frac{1}{2}\}$, and PT stands for the combined inversion symmetry P and time-reversal symmetry T. Then, the obtained irreps, written in the BCS convention [86,87], of H would be $H5 + H6$ and the effective Hamiltonian model $\mathcal{H}(\mathrm{k})$ for the emergent particle at the H point is constrained by $\Delta(\mathcal{O})\mathcal{H}(\mathrm{k})\Delta^{-1}(\mathcal{O}) = \mathcal{H}(\hat{\mathcal{O}}\mathrm{k})$ [88]. Here $\mathcal{O} \in \{S_3^+, C_{21}'', PT\}$ is one of the three operators and $\Delta(\mathcal{O})$ denotes the corresponding matrix representation at the H point [88]. The obtained model given in Ref. [88] shows that the set of bands whose irreps is $H5 + H6$ forms a fourfold nodal point, namely a Dirac point, as shown in Figs. 3(e) and 3(f). Besides, the intersections of bands Q1+Q3 and Q2+Q4 form the fourfold degenerate Dirac points DP2 locating at the high-symmetry line A-H, near the H point, as illustrated in Figs. 3(e) and 3(f).

Referring to Mg_3O, the intersections of the twofold bands LD1 and LD4 form DP along the M-K path. Combining with the inversion symmetry P, the time-reversal symmetry T, and the rotation symmetry C_{3z}^+ [88], there would be six DNLs in the whole BZ [see Fig. 3(m)]. The topology of DNLs can be further evaluated by the Berry phase in terms of $\gamma_n = \oint_C d\boldsymbol{R} \cdot A_n(\boldsymbol{R})$, in which C is a closed path encircling a generic point of the DNL and the vector $A_n(\boldsymbol{R})$ stands for the Berry connection [89]. Remarkably, each DNL generates a Berry phase of π, implying that each DNL is nontrivial. Besides, the acquired edge states for the DPs of Mg_3N and the DNLs of Mg_3O, which are projected to the (100) surface [Fig. 1(b)], are well demonstrated in Figs. 3(g) and 3(n), respectively.

It should be pointed out that when one takes excess electrons as interstitial quasiatoms [79,80,90,91], i.e., places ISQs at the 4c: $(\frac{1}{3}, \frac{2}{3}, \frac{3}{4})$ Wyckoff sites to construct

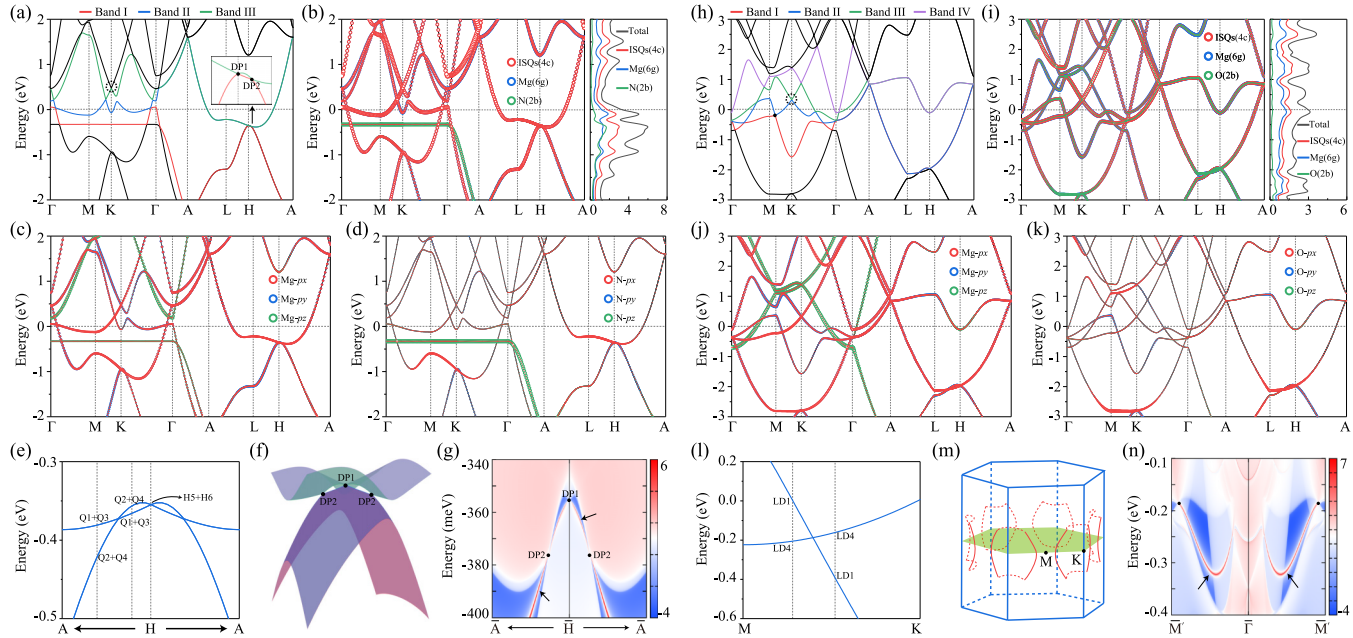

FIG. 3. Electronic structure and topological elements of Mg_3N (left panel) and Mg_3O (right panel). Band structure of Mg_3N (a) and Mg_3O (h). The bands crossing the Fermi level are highlighted by different colors. The inset in (a) is an enlarged view for the DP1 and DP2. The calculated projected band structure and density of states of Mg_3N (b) and Mg_3O (i). The orbital-resolved band structures of Mg_3N (c), (d) and Mg_3O (j), (k). The computed irreducible representations for the bands forming the topological elements of Mg_3N (e) and Mg_3O (l). Distribution of the DPs (f) and the DNLs (m). The topological surface states of Mg_3N (g) and Mg_3O (n), where the band crossings and edge states are indicated by the black solid circles and arrows, respectively.

kagome nets for Mg_3N and Mg_3O [see dashed lines in Figs. 2(b), 2(d), 2(f), and 2(h)], one can obtain projected band structures (PBANDS) and projected density of states (PDOS) including contributions from ISQs. Figures 3(b) and 3(i) suggest Mg and ISQs dominate the PBANDS and PDOS around the E_F, where the in-plane orbits (p_x and p_y) make a greater contribution than that of the out-of-plane orbits (p_z) for Mg, N, and O [Figs. 3(c), 3(d), 3(j), and 3(k)]. Interestingly, the above phenomena happen to coincide with the distribution of ELFs and PCDs in Fig. 2, that is, the localized electrons mostly lie in the plane of Mg layers (see also Fig. S3 [57]). Then, one may ask what about the atomic vibrations?

As shown in Figs. 4(a) and 4(c), the distinctive atomic vibration information can be roughly summarized as follows: the vibrations in low-frequency regions are dominantly originated from Mg atoms (0–40 meV for Mg_3N and 0–30 meV for Mg_3O); the medium-frequency vibrations mainly come from the Mg and nonmetal atoms (40–55 meV for Mg_3N and 30–50 meV for Mg_3O); and the high-frequency vibrations are dominated by N and O atoms (60–85 meV for Mg_3N and 50–70 meV for Mg_3O). Furthermore, combing with Figs. 4(b) and 4(d), it is clear that the superconducting parameter $\lambda_{\mathbf{q}\nu}$ mainly comes from the vibrations of Mg atoms, especially the in-plane vibrations. Moreover, the vibrations trigger some Eliashberg spectra function $\alpha^2F(\omega)$ peaks and subsequently form the accumulated EPC constants $\lambda(\omega)$. Meanwhile, combing with the ISQs distribution in Figs. 2 and 3, the interactions between the kagome lattice electrons (ISQs) and the in-plane vibration modes of Mg atoms may play an essential role in the EPC. Finally, according to the BCS theory, the superconducting parameters $\omega_{\log}$, λ, and T_c for Mg_3N (Mg_3O) are 234.8 (241.7) K, 0.46 (0.47), and 2.0 (2.2) K, respectively (Table I). Noticeably, the total EPC λ suggests the electron-phonon strength is weak in our predicated 2D kagome electrides [52–55] and the obtained T_{cs} are comparable to the reported superconducting electrides Li_5Si (∼1.1 K) [54], Li_5P (∼2.61 K) [52], Li_6P (∼2.87 K for the $P1$ phase) [52], Li_5C (∼3.1 K) [53], and Ba_2N (∼3.4 K) [55].

It is noticeable that the different electronic orbitals at the Fermi level could lead to the emergence of superconducting multigaps [92–95]. As shown in Fig. 3, several orbitals, such as p (p_x, p_y, and p_z) orbitals of Mg atoms, in-plane p (p_x and p_y) orbitals of O (N) atoms, and ISQs, emerge at the E_F, which means that the superconducting multigaps might be observed for Mg_3N and Mg_3O. However, it is quite costly and time consuming to obtain the superconducting multigaps, and here we will focus on the realization of kagome lattice and superconductivity in Mg_3N and Mg_3O.

Since the interplay between the charge density wave (CDW), the structural (electronic) instability, and the magnetism has been reported for kagome materials [4,74,93,96,97], we proceed with investigations for these properties. The results of the temperature-dependent AIMD simulations (1–300 K) (Fig. S4) [57] indicate these two proposed electrides are stable and will not undergo structural phase transition. Meanwhile, Mg_3N and Mg_3O are confirmed as nonmagnetic materials, which implies no magnetic phase transition. Moreover, there are no soft modes around the high-symmetry points or special routes in the phonon dispersion, suggesting the structural phase transition is absent. Finally, there are no flat band or van Hove singularity around the E_F (Fig. 3), and hence the Fermi nesting is absent in the

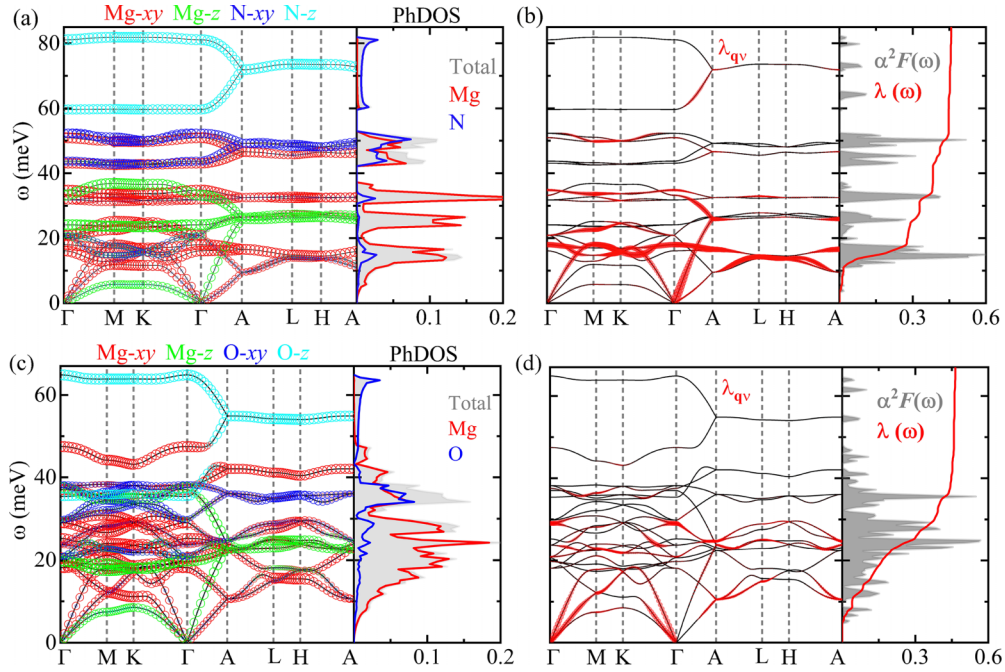

FIG. 4. Phonon and superconducting features of Mg_3N and Mg_3O. Phonon dispersion weighted by different atomic vibrational modes of Mg_3N (a) and Mg_3O (c). The right panels of (a) and (c) are the total (gray shaded zone) and vibrational mode-resolved (colored lines) phonon density of states (PhDOS). (b) and (d) demonstrate the phonon dispersion weighted by the magnitude of the EPC, the Eliashberg spectral function $\alpha^2F(\omega)$, and the integrated strength of EPC λ (ω).

Fermi surface (Fig. S5) [57]. Thus, there is no magnetism, no structural instability, or electronic instability in Mg_3N and Mg_3O, which indicates the CDW would be absent.

In the end, we evaluate the influence of pressure on the lattice displacement and superconductivity. For simplicity, we take Mg_3N as an example and the pressure is set to 5 GPa. The in-plane (Fig. S6), out-of-plane (Fig. S7), and hydrostatic pressure (Fig. S8) is respectively applied on Mg_3N [57]. The corresponding superconducting parameters $\omega_{\log}$, λ, and T_c are estimated to be 240, 205, 174 K, 0.44, 0.63, 0.66 and 1.7, 5.4, 5.3 K, respectively. The results suggest that the out-of-plane (along the c axis) pressure can effectively enhance the EPC strength λ and T_c. However, the in-plane (along the ab axes) pressure suppress them. Meanwhile, with the introduction of pressure, the values of $\omega_{\log}$ are decreasing. As depicted in Figs. S8 and S9, the in-plane vibrations of Mg and N atoms are more susceptible to the out-of-plane pressure, while the in-plane vibrations respond more slowly to the in-plane pressure. Moreover, as shown in Figs. S8–S10, the in-plane vibration of N atoms around 15 meV plays an essential role in the EPC under pressure, rather than the in-plane vibration of Mg atoms. The influence of different pressures on the superconductivity will be illustrated in the next work.

IV. CONCLUSION

In summary, kagome lattice and superconductivity were realized in the stable topological electrides Mg_3N and Mg_3O. Remarkably, the excess electrons donated by Mg atoms distribute within the Mg layers and construct the 2D kagome lattices. These ISQs contribute to the nontrival topological elements and take part in the interplay between the in-plane electronic orbitals and atomic vibrations that act as an important role in the EPC. The superconductivity in both systems are primarily contributed by the electronic states and phonon vibrations from the Mg atoms and the ISQs. This work proposes two stable superconducting electrides and supplies a potential playground to investigate the band topology and superconductivity in kagome electrides.

ACKNOWLEDGMENTS

M.Q.K. thanks helpful discussions with Y. Zhang, L. Liu, C. Wang, and T. Yu. We appreciate financial support from the National Natural Science Foundation of China (NSFC) with Grants No. 11704315, No. 12204074, No. 11675195, and No. 12074381. D.S.M. also thanks support from the China National Postdoctoral Program for Innovative Talent with Grant No. BX20220367. M.Q.K also appreciates support from the Natural Science Foundation of Chongqing with Grant No. 2024NSCQ-MSX3816. Part of the calculations were performed at CSNS Scientific Computing Platform of Institute of High Energy Physics of CAS and GBA Sub-center of National HEP Science Data Center.

[1] J.-X. Yin, B. Lian, and M. Z. Hasan, Topological kagome magnets and superconductors, Nature (London) **612**, 647 (2022).

[2] E. Liu, Y. Sun, N. Kumar, L. Muechler, A. Sun, L. Jiao, S.-Y. Yang, D. Liu, A. Liang, Q. Xu, J. Kroder, V. Süß, H. Borrmann, C. Shekhar, Z. Wang, C. Xi, W. Wang, W. Schnelle, S. Wirth, Y. Chen *et al.*, Giant anomalous Hall effect in a ferromagnetic kagome-lattice semimetal, Nat. Phys. **14**, 1125 (2018).

[3] X. Teng, L. Chen, F. Ye, E. Rosenberg, Z. Liu, J.-X. Yin, Y.-X. Jiang, J. S. Oh, M. Z. Hasan, K. J. Neubauer, B. Gao, Y. Xie, M. Hashimoto, D. Lu, C. Jozwiak, A. Bostwick, E. Rotenberg, R. J. Birgeneau, J.-H. Chu, M. Yi *et al.*, Discovery of charge density wave in a kagome lattice antiferromagnet, Nature (London) **609**, 490 (2022).

[4] X. Teng, J. S. Oh, H. Tan, L. Chen, J. Huang, B. Gao, J.-X. Yin, J.-H. Chu, M. Hashimoto, D. Lu, C. Jozwiak, A. Bostwick, E. Rotenberg, G. E. Granroth, B. Yan, R. J. Birgeneau, P. Dai, and M. Yi, Magnetism and charge density wave order in kagome FeGe, Nat. Phys. **19**, 814 (2023).

[5] M.-X. Wu, Y.-H. Wei, D.-S. Ma, P. Wang, N. Gao, S.-Y. Wu, and M.-Q. Kuang, In-plane canted ferromagnetism, intrinsic Weyl fermions, and large anomalous Hall effect in the kagome semimetal $Rh_3Sn_2S_2$, Phys. Rev. B **108**, 174430 (2023).

[6] T. Ahsan, C.-H. Hsu, M. S. Hossain, and M. Z. Hasan, Prediction of strong topological insulator phase in kagome metal RV_6Ge_6, Phys. Rev. Mater. **7**, 104204 (2023).

[7] H. D. Rosales, F. A. G. Albarracín, P. Pujol, and L. D. C. Jaubert, Skyrmion fluid and bimeron glass protected by a chiral spin liquid on a kagome lattice, Phys. Rev. Lett. **130**, 106703 (2023).

[8] D. Golovanova, H. Tan, T. Holder, and B. Yan, Tuning the intrinsic spin Hall effect by charge density wave order in topological kagome metals, Phys. Rev. B **108**, 205203 (2023).

[9] A. Lopez-Bezanilla, J. Raymond, K. Boothby, J. Carrasquilla, C. Nisoli, and A. D. King, Kagome qubit ice, Nat. Commun. **14**, 1105 (2023).

[10] X. Zhang, I.-A. Chioar, G. Fitez, A. Hurben, M. Saccone, N. S. Bingham, J. Ramberger, C. Leighton, C. Nisoli, and P. Schiffer, Artificial magnetic tripod ice, Phys. Rev. Lett. **131**, 126701 (2023).

[11] W. Zhu, S.-S. Gong, T.-S. Zeng, L. Fu, and D. N. Sheng, Interaction-driven spontaneous quantum Hall effect on a kagome lattice, Phys. Rev. Lett. **117**, 096402 (2016).

[12] H. Chen, H. Nassar, A. N. Norris, G. Hu, and G. L. Huang, Elastic quantum spin Hall effect in kagome lattices, Phys. Rev. B **98**, 094302 (2018).

[13] Y.-C. Lau, J. Ikeda, K. Fujiwara, A. Ozawa, J. Zheng, T. Seki, K. Nomura, L. Du, Q. Wu, A. Tsukazaki, and K. Takanashi, Intercorrelated anomalous Hall and spin Hall effect in kagome-lattice $Co_3Sn_2S_2$-based shandite films, Phys. Rev. B **108**, 064429 (2023).

[14] G. Zheng, C. Tan, Z. Chen, M. Wang, X. Zhu, S. Albarakati, M. Algarni, J. Partridge, L. Farrar, J. Zhou, W. Ning, M. Tian, M. S. Fuhrer, and L. Wang, Electrically controlled superconductor-to-failed insulator transition and giant anomalous Hall effect in kagome metal CsV_3Sb_5 nanoflakes, Nat. Commun. **14**, 678 (2023).

[15] X. Li, J. Koo, Z. Zhu, K. Behnia, and B. Yan, Field-linear anomalous Hall effect and berry curvature induced by spin chirality in the kagome antiferromagnet Mn_3Sn, Nat. Commun. **14**, 1642 (2023).

[16] L. Ye, M. Kang, J. Liu, F. Von Cube, C. R. Wicker, T. Suzuki, C. Jozwiak, A. Bostwick, E. Rotenberg, D. C. Bell, L. Fu, R. Comin, and J. G. Checkelsky, Massive Dirac fermions in a ferromagnetic kagome metal, Nature (London) **555**, 638 (2018).

[17] D. Liu, A. Liang, E. Liu, Q. Xu, Y. Li, C. Chen, D. Pei, W. Shi, S. Mo, P. Dudin, T. Kim, C. Cacho, G. Li, Y. Sun, L. Yang, Z. Liu, S. Parkin, C. Felser, and Y. Chen, Magnetic Weyl semimetal phase in a Kagomé crystal, Science **365**, 1282 (2019).

[18] M. Kang, L. Ye, S. Fang, J.-S. You, A. Levitan, M. Han, J. I. Facio, C. Jozwiak, A. Bostwick, E. Rotenberg, D. C. Bell, E. Kaxiras, J. v. d. Brink, M. Richter, M. P. Ghimire, J. G. Checkelsky, and R. Comin, Dirac fermions and flat bands in the ideal kagome metal FeSn, Nat. Mater. **19**, 163 (2020).

[19] M. Kang, S. Fang, L. Ye, H. C. Po, J. Denlinger, C. Jozwiak, A. Bostwick, E. Rotenberg, E. Kaxiras, J. G. Checkelsky, and R. Comin, Topological flat bands in frustrated kagome lattice CoSn, Nat. Commun. **11**, 4004 (2020).

[20] M. Kang, S. Fang, J.-K. Kim, B. R. Ortiz, S. H. Ryu, J. Kim, J. Yoo, G. Sangiovanni, D. Di Sante, B.-G. Park, C. Jozwiak, A. Bostwick, E. Rotenberg, E. Kaxiras, S. D. Wilson, J.-H. Park, and R. Comin, Twofold van Hove singularity and origin of charge order in topological kagome superconductor CsV_3Sb_5, Nat. Phys. **18**, 301 (2022).

[21] J. Yang, X. Yi, Z. Zhao, Y. Xie, T. Miao, H. Luo, H. Chen, B. Liang, W. Zhu, Y. Ye, X.-Y. You, B. Gu, S. Zhang, F. Zhang, F. Yang, Z. Wang, Q. Peng, H. Mao, G. Liu, Z. Xu *et al.*, Observation of flat band, Dirac nodal lines and topological surface states in kagome superconductor $CsTi_3Bi_5$, Nat. Commun. **14**, 4089 (2023).

[22] S. Zhou and Z. Wang, Chern Fermi pocket, topological pair density wave, and charge-4e and charge-6e superconductivity in Kagomé superconductors, Nat. Commun. **13**, 7288 (2022).

[23] H. Li, D. Oh, M. Kang, H. Zhao, B. R. Ortiz, Y. Oey, S. Fang, Z. Ren, C. Jozwiak, A. Bostwick, E. Rotenberg, J. G. Checkelsky, Z. Wang, S. D. Wilson, R. Comin, and I. Zeljkovic, Small Fermi pockets intertwined with charge stripes and pair density wave order in a kagome superconductor, Phys. Rev. X **13**, 031030 (2023).

[24] Z. Liang, X. Hou, F. Zhang, W. Ma, P. Wu, Z. Zhang, F. Yu, J.-J. Ying, K. Jiang, L. Shan, Z. Wang, and X.-H. Chen, Three-dimensional charge density wave and surface-dependent vortex-core states in a kagome superconductor CsV_3Sb_5, Phys. Rev. X **11**, 031026 (2021).

[25] H. W. S. Arachchige, W. R. Meier, M. Marshall, T. Matsuoka, R. Xue, M. A. McGuire, R. P. Hermann, H. Cao, and D. Mandrus, Charge density wave in kagome lattice intermetallic ScV_6Sn_6, Phys. Rev. Lett. **129**, 216402 (2022).

[26] L. Zheng, Z. Wu, Y. Yang, L. Nie, M. Shan, K. Sun, D. Song, F. Yu, J. Li, D. Zhao, S. Li, B. Kang, Y. Zhou, K. Liu, Z. Xiang, J. Ying, Z. Wang, T. Wu, and X. Chen, Emergent charge order in pressurized kagome superconductor CsV_3Sb_5, Nature (London) **611**, 682 (2022).

[27] L. Nie, K. Sun, W. Ma, D. Song, L. Zheng, Z. Liang, P. Wu, F. Yu, J. Li, M. Shan, D. Zhao, S. Li, B. Kang, Z. Wu, Y. Zhou, K. Liu, Z. Xiang, J. Ying, Z. Wang, T. Wu *et al.*, Charge-density-wave-driven electronic nematicity in a kagome superconductor, Nature (London) **604**, 59 (2022).

[28] H. Miao, T. Zhang, H. Li, G. Fabbris, A. Said, R. Tartaglia, T. Yilmaz, E. Vescovo, J.-X. Yin, S. Murakami, X. Feng, K. Jiang,

X. Wu, A. Wang, S. Okamoto, Y. Wang, and H. Lee, Signature of spin-phonon coupling driven charge density wave in a kagome magnet, Nat. Commun. **14**, 6183 (2023).

[29] J. T. Chalker, P. C. Holdsworth, and E. F. Shender, Hidden order in a frustrated system: Properties of the Heisenberg Kagomé antiferromagnet, Phys. Rev. Lett. **68**, 855 (1992).

[30] J. N. Reimers and A. J. Berlinsky, Order by disorder in the classical Heisenberg Kagomé antiferromagnet, Phys. Rev. B **48**, 9539 (1993).

[31] H. Zhao, H. Li, B. R. Ortiz, S. M. Teicher, T. Park, M. Ye, Z. Wang, L. Balents, S. D. Wilson, and I. Zeljkovic, Cascade of correlated electron states in the kagome superconductor CsV_3Sb_5, Nature (London) **599**, 216 (2021).

[32] T. Neupert, M. M. Denner, J.-X. Yin, R. Thomale, and M. Z. Hasan, Charge order and superconductivity in kagome materials, Nat. Phys. **18**, 137 (2022).

[33] J.-G. Si, L.-T. Shi, P.-F. Liu, P. Zhang, and B.-T. Wang, Superconductivity and topological properties in the kagome metals CsM_3Te_5 (M = Ti, Zr, Hf): A first-principles investigation, Phys. Rev. B **106**, 214527 (2022).

[34] D.-B. Zha, P. Jiang, H.-M. Huang, and Y.-L. Li, Refined phase diagram and kagome-lattice superconductivity in Mg-Si system, Phys. Rev. Mater. **7**, 114805 (2023).

[35] L.-T. Shi, J.-G. Si, A. Liang, R. Turnbull, P.-F. Liu, and B.-T. Wang, Topological and superconducting properties in bilayer kagome metals YT_6Sn_6 (T = V, Nb, Ta), Phys. Rev. B **107**, 184503 (2023).

[36] H. Chen, H. Yang, B. Hu, Z. Zhao, J. Yuan, Y. Xing, G. Qian, Z. Huang, G. Li, Y. Ye, S. Ma, S. Ni, H. Zhang, Q. Yin, C. Gong, Z. Tu, H. Lei, H. Tan, S. Zhou, C. Shen *et al.*, Roton pair density wave in a strong-coupling kagome superconductor, Nature (London) **599**, 222 (2021).

[37] B. Liu, M.-Q. Kuang, Y. Luo, Y. Li, C. Hu, J. Liu, Q. Xiao, X. Zheng, L. Huai, S. Peng, Y. Yao, Z. Wang, and J. He, Tunable van hove singularity without structural instability in kagome metal $CsTi_3Bi_5$, Phys. Rev. Lett. **131**, 026701 (2023).

[38] Y. Zhang, Y. Sun, H. Yang, J. Železný, S. P. P. Parkin, C. Felser, and B. Yan, Strong anisotropic anomalous Hall effect and spin Hall effect in the chiral antiferromagnetic compounds Mn_3X (X= Ge, Sn, Ga, Ir, Rh, and Pt), Phys. Rev. B **95**, 075128 (2017).

[39] Z. Lin, J.-H. Choi, Q. Zhang, W. Qin, S. Yi, P. Wang, L. Li, Y. Wang, H. Zhang, Z. Sun, L. Wei, S. Zhang, T. Guo, Q. Lu, J.-H. Cho, C. Zeng, and Z. Zhang, Flatbands and emergent ferromagnetic ordering in Fe_3Sn_2 kagome lattices, Phys. Rev. Lett. **121**, 096401 (2018).

[40] B. P. Belbase, L. Ye, B. Karki, J. I. Facio, J.-S. You, J. G. Checkelsky, J. Van Den Brink, and M. P. Ghimire, Large anomalous Hall effect in single crystals of the kagome Weyl ferromagnet Fe_3Sn, Phys. Rev. B **108**, 075164 (2023).

[41] A. Carlsson, J. Rosen, and M. Dahlqvist, Finding stable multi-component materials by combining cluster expansion and crystal structure predictions, npj Comput. Mater. **9**, 21 (2023).

[42] S. Chaudhary, Shama, J. Singh, A. Consiglio, D. Di Sante, R. Thomale, and Y. Singh, Role of electronic correlations in the kagome-lattice superconductor $LaRh_3B_2$, Phys. Rev. B **107**, 085103 (2023).

[43] Y. Ma, M. Eremets, A. R. Oganov, Y. Xie, I. Trojan, S. Medvedev, A. O. Lyakhov, M. Valle, and V. Prakapenka, Transparent dense sodium, Nature (London) **458**, 182 (2009).

[44] T.-N. Ye, S.-W. Park, Y. Lu, J. Li, M. Sasase, M. Kitano, T. Tada, and H. Hosono, Vacancy-enabled N_2 activation for ammonia synthesis on an Ni-loaded catalyst, Nature (London) **583**, 391 (2020).

[45] W. Meng, X. Zhang, Y. Liu, X. Dai, G. Liu, Y. Gu, E. Kenny, and L. Kou, Multifold fermions and fermi arcs boosted catalysis in nanoporous electride $12CaO \cdot 7Al_2O_3$, Adv. Sci. **10**, 2205940 (2023).

[46] S. Bae, W. Espinosa-García, Y.-G. Kang, N. Egawa, J. Lee, K. Kuwahata, M. Khazaei, K. Ohno, Y.-H. Kim, M. J. Han, H. Hosono, G. M. Dalpian, and H. Raebiger, Mxene phase with C_3 structure unit: A family of 2D electrides, Adv. Funct. Mater. **31**, 2100009 (2021).

[47] Y. Chen, H. Qin, J. Zhou, T. Yang, B. Sun, Y. Ni, H. Wang, S. A. Redfern, M. Miao, H.-Q. Lin, and Y. P. Feng, Unveiling interstitial anionic electron-driven ultrahigh K-ion storage capacity in a novel two-dimensional electride exemplified by Sc_3Si_2, J. Phys. Chem. Lett. **13**, 7439 (2022).

[48] R.-L. Zhong, H.-L. Xu, Z.-R. Li, and Z.-M. Su, Role of excess electrons in nonlinear optical response, J. Phys. Chem. Lett. **6**, 612 (2015).

[49] Q. Chen, X. Zheng, P. Jiang, Y.-H. Zhou, L. Zhang, and Z. Zeng, Electric field induced tunable half-metallicity in an A-type antiferromagnetic bilayer $LaBr_2$, Phys. Rev. B **106**, 245423 (2022).

[50] J. Zhou, Z. Wang, S. Wang, Y. P. Feng, M. Yang, and L. Shen, Coexistence of ferromagnetism and charge density waves in monolayer $LaBr_2$, Nanoscale Horiz. **8**, 1054 (2023).

[51] M. Miyakawa, S. W. Kim, M. Hirano, Y. Kohama, H. Kawaji, T. Atake, H. Ikegami, K. Kono, and H. Hosono, Superconductivity in an inorganic electride $12CaO7Al_2O_3{:}e^-$, J. Am. Chem. Soc. **129**, 7270 (2007).

[52] Z. Zhao, S. Zhang, T. Yu, H. Xu, A. Bergara, and G. Yang, Predicted pressure-induced superconducting transition in electride Li_6P, Phys. Rev. Lett. **122**, 097002 (2019).

[53] Z. S. Pereira, G. M. Faccin, and E. Z. da Silva, Predicted superconductivity in the electride Li_5C, J. Phys. Chem. C **125**, 8899 (2021).

[54] J.-Y. You, B. Gu, G. Su, and Y. P. Feng, Emergent kagome electrides, J. Am. Chem. Soc. **144**, 5527 (2022).

[55] X.-L. Qiu, J.-F. Zhang, H.-C. Yang, Z.-Y. Lu, and K. Liu, Superconductivity in monolayer Ba_2N electride: First-principles study, Phys. Rev. B **105**, 165101 (2022).

[56] Z. Chen, T. Xie, P.-F. Liu, R. Xiong, Z. Cui, Z. Xu, C. Wen, B.-T. Wang, and B. Sa, Superconductivity in Ca_3H_2 electride at moderate pressure, J. Mater. Chem. C **11**, 16728 (2023).

[57] See Supplemental Material at http://link.aps.org/supplemental/10.1103/PhysRevB.110.054511 for the following: The phonon spectra and AIMD simulations for Mg_3N and Mg_3O; The formation energy of Mg_xN_{1-x} and Mg_xO_{1-x}; The PCD for Mg_3N and Mg_3O with a same isovalue; The AIMD simulations of Mg_3N and Mg_3O from 1–300 K; The Fermi surface of Mg_3N and Mg_3O; The effect of in-plane pressure on lattice vibration and superconductivity for Mg_3N; The effect of out-of-plane pressure on lattice vibration and superconductivity for Mg_3N; and the effect of hydrostatic pressure on lattice vibration and superconductivity for Mg_3N, which includes Refs. [76,77].

[58] W. McMillan, Transition temperature of strong-coupled superconductors, Phys. Rev. **167**, 331 (1968).

[59] P. B. Allen and R. Dynes, Transition temperature of strong-coupled superconductors reanalyzed, Phys. Rev. B **12**, 905 (1975).

[60] G. Kresse and J. Hafner, *Ab initio* molecular-dynamics simulation of the liquid-metal–amorphous-semiconductor transition in germanium, Phys. Rev. B **49**, 14251 (1994).

[61] G. Kresse and J. Furthmüller, Efficient iterative schemes for *ab initio* total-energy calculations using a plane-wave basis set, Phys. Rev. B **54**, 11169 (1996).

[62] P. E. Blöchl, Projector augmented-wave method, Phys. Rev. B **50**, 17953 (1994).

[63] J. P. Perdew, K. Burke, and M. Ernzerhof, Generalized gradient approximation made simple, Phys. Rev. Lett. **77**, 3865 (1996).

[64] A. Togo and I. Tanaka, First principles phonon calculations in materials science, Scr. Mater. **108**, 1 (2015).

[65] S. Baroni, S. De Gironcoli, A. Dal Corso, and P. Giannozzi, Phonons and related crystal properties from density-functional perturbation theory, Rev. Mod. Phys. **73**, 515 (2001).

[66] Q. Wu, S. Zhang, H.-F. Song, M. Troyer, and A. A. Soluyanov, Wanniertools: An open-source software package for novel topological materials, Comput. Phys. Commun. **224**, 405 (2018).

[67] I. Souza, N. Marzari, and D. Vanderbilt, Maximally localized Wannier functions for entangled energy bands, Phys. Rev. B **65**, 035109 (2001).

[68] N. Marzari, A. A. Mostofi, J. R. Yates, I. Souza, and D. Vanderbilt, Maximally localized Wannier functions: Theory and applications, Rev. Mod. Phys. **84**, 1419 (2012).

[69] M. J. Verstraete, M. Torrent, F. Jollet, G. Zérah, and X. Gonze, Density functional perturbation theory with spin-orbit coupling: Phonon band structure of lead, Phys. Rev. B **78**, 045119 (2008).

[70] P. Giannozzi, S. Baroni, N. Bonini, M. Calandra, R. Car, C. Cavazzoni, D. Ceresoli, G. L. Chiarotti, M. Cococcioni, I. Dabo, A. Dal Corso, S. de Gironcoli, S. Fabris, G. Fratesi, R. Gebauer, U. Gerstmann, C. Gougoussis, A. Kokalj, M. Lazzeri, L. Martin-Samos *et al.*, QUANTUM ESPRESSO: a modular and open-source software project for quantum simulations of materials, J. Phys.: Condens. Matter **21**, 395502 (2009).

[71] P. B. Allen and B. Mitrović, Theory of superconducting T_c, Solid State Phys. **37**, 1 (1983).

[72] E. R. Margine and F. Giustino, Anisotropic Migdal-Eliashberg theory using Wannier functions, Phys. Rev. B **87**, 024505 (2013).

[73] J. Kortus, I. Mazin, K. D. Belashchenko, V. P. Antropov, and L. Boyer, Superconductivity of metallic boron in MgB_2, Phys. Rev. Lett. **86**, 4656 (2001).

[74] J.-G. Si, W.-J. Lu, Y.-P. Sun, P.-F. Liu, and B.-T. Wang, Charge density wave and pressure-dependent superconductivity in the kagome metal CsV_3Sb_5: A first-principles study, Phys. Rev. B **105**, 024517 (2022).

[75] C. Park, S. W. Kim, and M. Yoon, First-principles prediction of new electrides with nontrivial band topology based on one-dimensional building blocks, Phys. Rev. Lett. **120**, 026401 (2018).

[76] J. E. Saal, S. Kirklin, M. Aykol, B. Meredig, and C. Wolverton, Materials design and discovery with high-throughput density functional theory: the open quantum materials database (OQMD), JOM **65**, 1501 (2013).

[77] S. Kirklin, J. E. Saal, B. Meredig, A. Thompson, J. W. Doak, M. Aykol, S. Rühl, and C. Wolverton, The open quantum materials database (OQMD): assessing the accuracy of dft formation energies, npj Comput. Mater. **1**, 15010 (2015).

[78] W. M. Haynes, *CRC Handbook of Chemistry and Physics* (CRC Press, Boca Raton, 2016).

[79] Y. Zhang, W. Wu, Y. Wang, S. A. Yang, and Y. Ma, Pressure-stabilized semiconducting electrides in alkaline-earth-metal subnitrides, J. Am. Chem. Soc. **139**, 13798 (2017).

[80] Y. Zhang, H. Wang, Y. Wang, L. Zhang, and Y. Ma, Computer-assisted inverse design of inorganic electrides, Phys. Rev. X **7**, 011017 (2017).

[81] Q. Zhu, T. Frolov, and K. Choudhary, Computational discovery of inorganic electrides from an automated screening, Matter **1**, 1293 (2019).

[82] J. L. Dye, Electrons as anions, Science **301**, 607 (2003).

[83] G. Wang, Z. Ma, J.-W. Jiang, J.-k. Yang, Y.-L. Sun, Z.-F. Qian, P. Huang, P. Zhang, and S.-H. Wei, Crystal structures and physicochemical properties of Be_2N and Mg_2N as electride materials, Phys. Rev. Appl. **19**, 034014 (2023).

[84] S. Zhang, M. Kang, H. Huang, W. Jiang, X. Ni, L. Kang, S. Zhang, H. Xu, Z. Liu, and F. Liu, kagome bands disguised in a coloring-triangle lattice, Phys. Rev. B **99**, 100404 (2019).

[85] J. Gao, Q. Wu, C. Persson, and Z. Wang, Irvsp: To obtain irreducible representations of electronic states in the VASP, Comput. Phys. Commun. **261**, 107760 (2021).

[86] M. I. Aroyo, A. Kirov, C. Capillas, J. Perez-Mato, and H. Wondratschek, Bilbao Crystallographic Server. II. Representations of crystallographic point groups and space groups, Acta Crystallogr., Sect. A: Found. Crystallogr. **62**, 115 (2006).

[87] L. Elcoro, B. Bradlyn, Z. Wang, M. G. Vergniory, J. Cano, C. Felser, B. A. Bernevig, D. Orobengoa, G. Flor, and M. I. Aroyo, Double crystallographic groups and their representations on the Bilbao Crystallographic Server, J. Appl. Crystallogr. **50**, 1457 (2017).

[88] Z.-M. Yu, Z. Zhang, G.-B. Liu, W. Wu, X.-P. Li, R.-W. Zhang, S. A. Yang, and Y. Yao, Encyclopedia of emergent particles in three-dimensional crystals, Sci. Bull. **67**, 375 (2022).

[89] D. Xiao, M.-C. Chang, and Q. Niu, Berry phase effects on electronic properties, Rev. Mod. Phys. **82**, 1959 (2010).

[90] K. Lee, S. W. Kim, Y. Toda, S. Matsuishi, and H. Hosono, Dicalcium nitride as a two-dimensional electride with an anionic electron layer, Nature (London) **494**, 336 (2013).

[91] S. Y. Lee, J.-Y. Hwang, J. Park, C. N. Nandadasa, Y. Kim, J. Bang, K. Lee, K. H. Lee, Y. Zhang, Y. Ma, H. Hosono, Y. H. Lee, S.-G. Kim, and S. W. Kim, Ferromagnetic quasi-atomic electrons in two-dimensional electride, Nat. Commun. **11**, 1526 (2020).

[92] J. Bekaert, A. Aperis, B. Partoens, P. M. Oppeneer, and M. V. Milošević, Evolution of multigap superconductivity in the atomically thin limit: Strain-enhanced three-gap superconductivity in monolayer MgB_2, Phys. Rev. B **96**, 094510 (2017).

[93] F. Zheng and J. Feng, Electron-phonon coupling and the coexistence of superconductivity and charge-density wave in monolayer $NbSe_2$, Phys. Rev. B **99**, 161119 (2019).

[94] Y. Zhao, C. Lian, S. Zeng, Z. Dai, S. Meng, and J. Ni, MgB_4 trilayer film: A four-gap superconductor, Phys. Rev. B **101**, 104507 (2020).

[95] L. Liu, X. Liu, P. Song, L. Zhang, X. Huang, W. Zhang, Z. Zhang, and Y. Jia, Surface superconductivity with high

transition temperatures in layered $Ca_nB_{n+1}C_{n+1}$ films, Nano Lett. **23**, 1924 (2023).

[96] J. G. Si, W. J. Lu, H. Y. Wu, H. Y. Lv, X. Liang, Q. J. Li, and Y. P. Sun, Origin of the multiple charge density wave order in $1T - VSe_2$, Phys. Rev. B **101**, 235405 (2020).

[97] H. Tan and B. Yan, Abundant lattice instability in kagome metal ScV_6Sn_6, Phys. Rev. Lett. **130**, 266402 (2023).